Intrinsic doping limit and defect-assisted luminescence in Cs_4PbBr_6

Young-Kwang Jung,[†] Joaquín Calbo,[‡] Ji-Sang Park,[‡] Lucy D. Whalley,[‡] Sunghyun Kim,[‡] and Aron Walsh[*,†,‡]

†*Department of Materials Science and Engineering, Yonsei University, Seoul 03722, Korea*

‡*Department of Materials, Imperial College London, Exhibition Road, London SW7 2AZ, UK*

E-mail: a.walsh@imperial.ac.uk

Abstract

Cs_4PbBr_6 is a member of the halide perovskite family that is built from isolated (zero-dimensional) $PbBr_6^{4-}$ octahedra with Cs^+ counter ions. The material exhibits anomalous optoelectronic properties: optical absorption and weak emission in the deep ultraviolet (310 – 375 nm) with efficient luminescence in the green region ($\sim$ 540 nm). Several hypotheses have been proposed to explain the giant Stokes shift including: (i) phase impurities; (ii) self-trapped exciton; (iii) defect emission. We explore, using first-principles theory and self-consistent Fermi level analysis, the unusual defect chemistry and physics of Cs_4PbBr_6. We find a heavily compensated system where the room-temperature carrier concentrations ($< 10^9\,cm^{-3}$) are more than one million times lower than the defect concentrations. We show that the low-energy Br-on-Cs antisite results in the formation of a polybromide (Br_3) species that can exist in a range of charge states. We further demonstrate from excited-state calculations that tribromide moieties are photoresponsive and can contribute to the observed green luminescence. Photoactivity of polyhalide molecules is expected to be present in other

halide perovskite-related compounds where they can influence light absorption and emission.

Introduction

Defects in solids can absorb and emit radiation with optical lines as narrow as $1\,\mathrm{cm}^{-1}$.[1] When it comes to wide band gap semiconductors and dielectrics, defect luminescence enables a single material to emit photons across the visible range, e.g. red emission in ZnO,[2] blue emission in GaN,[3] and the range of F-centers in alkali halides.[4] In contrast to established systems, defect processes in the new generation of halide perovskite inspired compounds are poorly understood with little quantitative information on the identity and concentrations of electrically and optically active centres.[5]

Conventional ABX_3 halide perovskites are based on corner-sharing networks of BX_6 octahedra in 3D, while layered 2D networks have also been intensively studied for application in solar cells.[6–8] The family of A_4BX_6 compounds, so called 0D perovskites, containing isolated octahedra, however, have attracted significant research attention recently due to their unique crystal structure and opto-electronic properties.[9,10] These ternary compounds can be formed by the reaction of the two corresponding binary halides:

$$4\,AX + BX_2 \rightleftharpoons A_4BX_6 \tag{1}$$

which is achieved under AX-rich growth conditions.

As a member of the ABX_3 family, Cs_4PbBr_6 has been the subject of attention due to its high photoluminescence quantum yield (PLQY) at green wavelengths and long-term stability.[9,11] In 1983, the absorption edge of Cs_4PbBr_6 was firstly reported as $2.34\,\mathrm{eV}$,[12] and later different optical properties of Cs_4PbBr_6 bulk and thin film samples were revealed.[13] While the thin film sampled showed absorption and emission features around the ultra-violet (UV) region, the bulk sample showed activity around the green visible-light region. Since

another phase of Cs_4PbBr_6, namely $CsPbBr_3$, has a band gap in the green region, it has been believed that green PL of Cs_4PbBr_6 is due to $CsPbBr_3$ phase impurity. In addition, a recent report showed a high PLQY of up to 97 % for $CsPbBr_3$ nanocrystals embedded in a Cs_4PbBr_6 host.[14,15] Meanwhile, it was claimed that pure Cs_4PbBr_6 single crystals also emit green light with considerable PLQY.[16,17] Native defects of Cs_4PbBr_6 were speculated to cause green emission. However, direct evidence of defect-assisted green emission has not been reported. Hence, active debate on the origin of green luminescence of Cs_4PbBr_6 is ongoing.[18–21]

In this investigation, we critically assess existing hypotheses on defect formation and luminescence in Cs_4PbBr_6 with relevance to other 0D 4:1:6 perovskites. Based on a first-principles description of point defect reactions, including self-consistent Fermi level analysis to predict equilibrium defect concentrations, we find unusually strong charge compensation in this systems that severely limits the free charge carrier concentration. We show that bromine vacancies have a high-formation energy (negligible concentrations) in these systems and suggest an alternative complementary defect-assisted luminescence process involving the photochemistry of tribromide complexes.

Results and Discussion

Structural and electronic properties of Cs_4PbBr_6

The structure of the Cs_4PbBr_6 rhombohedral cell with space group $R\bar{3}c$ (167) is shown in Figure 1a. Cs atoms are at **2a** and **6e** Wyckoff positions, while Pb and Br atoms are at **2b** and **12f**, respectively. $PbBr_6$ octahedra are isolated by surrounding Cs atoms; there is direct connectivity between octahedra. The calculated bulk parameters of $a_0 = 13.61$ Å, $c_0 = 17.16$ Å for the conventional (hexagonal setting) cell agree with previous reports.[22,23] The bulk modulus of $B_0 = 12.1$ GPa for Cs_4PbBr_6 was obtained from fitting to the third-order Birch-Murnaghan equation-of-state,[24] which suggests 0D Cs_4PbBr_6 is much softer than 3D

$CsPbBr_3$ (21.5 GPa).[25]

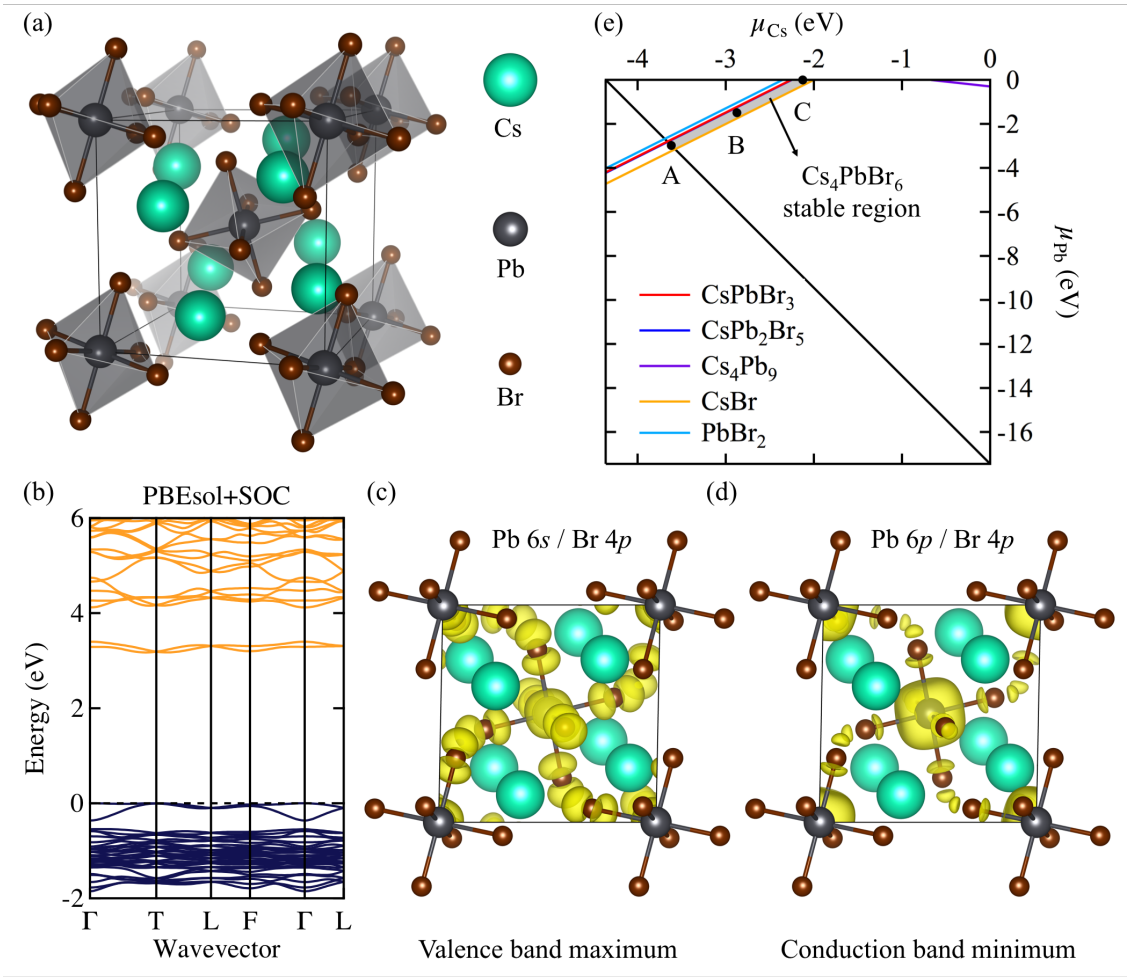

Figure 1: (a) Crystal structure representation of Cs_4PbBr_6. (b) Electronic band structure along the high symmetry lines of the first Brillouin zone. Orbital character in the (c) upper valence band and (d) lower conduction band. (e) Calculated stability field in chemical potential space, where the stable region for Cs_4PbBr_6 is shaded gray.

The calculated band gaps within density functional theory (DFT) at the (semi-local) PBEsol+SOC and (non-local) HSE06+SOC levels of theory are 3.20 eV and 4.11 eV, respectively. The HSE06+SOC band gap is comparable to the absorption peak position of 310 nm (4.00 eV) from Cs_4PbBr_6 thin film at room temperature.[13] This material shows flat band structure (Figure 1b) where upper valence bands are composed of Pb 6*s* and Br 4*p* whereas the lower conduction bands are comprised of Pb 6*p* and Br 4*p* (also see Figure S1). The flat band structure is associated with spatial confinement of the upper valence band and lower

conduction band wavefunctions within individual octahedra as shown in Figure 1c and 1d. The octahedra are electronically isolated and, consequently, charge carriers may localize. The effective masses for both electrons and holes are calculated to be heavy with $m_e^* = 2.94\, m_e$ and $m_h^* = 3.29\, m_e$, in contrast to $m_e^* < 0.2\, m_e$ found for 3D lead halide perovskites. [26]

A small value for the static dielectric constant (ϵ_0) of 8.02 was obtained from density functional perturbation theory,[27] arising from the sum of the ionic contribution ($\epsilon_{\text{ionic}} = 4.81$) and optical dielectric constant ($\epsilon_\infty = 3.21$). We note that the combination of high carrier effective masses and low dielectric constant of Cs_4PbBr_6 is opposite to the low carrier effective masses and high dielectric constants of many 3D hybrid perovskites.[28,29]

Electronic alignment between Cs_4PbBr_6 and $CsPbBr_3$

To assess the role of phase impurities in light emission, we calculated the absolute electron energies of the valence band maximum (VBM) and conduction band minimum (CBM) of Cs_4PbBr_6 following the procedures outlined in Ref. 30. The VBM and CBM energies (HSE06+SOC) are $-5.68\,$eV and $-1.56\,$eV with respect to the vacuum level of non-polar $Cs_4PbBr_6(110)$ surface, which has a low surface energy of $6.99\,\text{meV/Å}^2$. The ionization potential matches well with measurements for Cs_4PbBr_6 nanocrystals of $-5.73\,$eV by Zhang et al. where the (110) surface is exposed.[31] Further details of our surface model are found in the Supporting Information (SI).

A range of band energies have been reported experimentally for $CsPbBr_3$ as shown in Figure 2.[32–35] Natural band alignment between Cs_4PbBr_6 and $CsPbBr_3$ displays formation of weak type I or II heterojunction depending on the reported values. Here, the valence band offset is found to be subtle (max. $\pm 0.3\,$eV). Since natural band alignment neglects effects of the specific interface (e.g. built-in potential which can shift the type of band alignment),[25,36] band alignment at an actual $CsPbBr_3/Cs_4PbBr_6$ mixture might differ depending on crystal orientation, stoichiometry, and structure matching across the interface. Thus, further study on the interface is required to obtain a quantitative band alignment to describe $CsPbBr_3$-

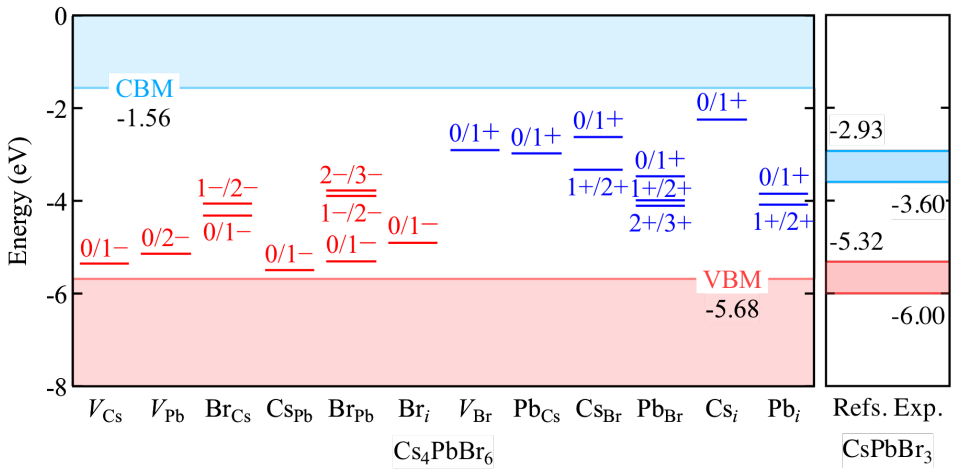

Figure 2: The natural electronic band alignment with respect to vacuum level (set to 0 eV). Range of reported $CsPbBr_3$ valence band maximum (VBM) and conduction band minimum (CBM) values are shown for comparison as taken from Refs. 32–35. The thermodynamic defect transition levels for each point defect are marked in red (acceptor defect) and blue (donor defect) dashes with respect to the valence and conduction bands of Cs_4PbBr_6.

assisted green emission. However, many recent reports, e.g. increase of PLQY by $CsPbBr_3$ embedded Cs_4PbBr_6 and similar photo-response between Cs_4PbBr_6 and $CsPbBr_3$, still indicate that $CsPbBr_3$ can act as a radiative recombination center for green emission if they co-exist.[11,14–16,20,37]

Thermodynamics of point defect formation

In order for defects to make an appreciable contribution to light absorption and emission, there needs to be a high population of an active species. When considering a single point defect, the equilibrium concentration (n_d) present in a crystal is simply determined by

$$n_d = N_d \exp\left(-\frac{\Delta G_d}{k_B T}\right) \tag{2}$$

where N_d is the specific lattice site concentration, ΔG_d is the Gibbs free energy of defect formation, k_B is Boltzmann constant, and T is temperature. Within the modern first-principles theory of defects, vibrational entropy is often neglected and ΔG_d is replaced by

the enthalpy of defect formation (ΔH_d), which can be calculated following

$$\Delta H_d(\alpha,\, q) = E(\alpha,\, q) - E(\text{host}) + \sum_i n_i(E_i + \mu_i) + q\,[E_{\text{VBM}} + E_{\text{F}}] + E_{\text{corr}} \tag{3}$$

where $E(\alpha,\, q)$ and $E(\text{host})$ are total energy of a supercell with point defect α in charge state q and a perfect supercell, respectively. E_i is the total energy of the standard state for element i, which is the reference for μ_i, while n_i is the number of i atoms exchanged with the thermodynamic reservoir when defect α forms. E_{F} is the Fermi level (electronic chemical potential) referenced to the VBM of the host Cs_4PbBr_6 (E_{VBM}), and E_{corr} is a finite-size electrostatic correction term. Note that the defect formation energy and hence the equilibrium populations are dependent on the atomic chemical potential and Fermi level.[5,38,39]

In addition to the reaction pathway for Cs_4PbBr_6 involving the binary halides (Eqn. 1, $\Delta H_f^{calc} = -0.43\,\text{eV}$), there is an equilibrium involving the 3D perovskite $CsPbBr_3$, including the disproportionation reactions:

$$CsPbBr_3 + 3\,CsBr \longrightarrow Cs_4PbBr_6 \tag{4}$$

$$Cs_4PbBr_6 + 3\,PbBr_2 \longrightarrow 4\,CsPbBr_3 \tag{5}$$

which have $\Delta H_f^{calc} = -0.26\,\text{eV}$ (Eqn. 4) and $-0.38\,\text{eV}$ (Eqn. 5), respectively. This implies that the coexistence of Cs_4PbBr_6 and $CsPbBr_3$ is possible, depending on local environment of precursors. Accordingly, phase competition in the Cs–Pb–Br system results in a narrow stability field for Cs_4PbBr_6 in chemical potential space where *bcc* Cs, *fcc* Pb, and solid Br are regarded as reference states (shown in Figure 1e with further details in the SI). These findings are consistent with observations that Cs_4PbBr_6 samples often contain CsBr or $CsPbBr_3$ secondary phases.[15,40]

Within the Cs_4PbBr_6 stable region on the chemical potential space (Figure 1e), we sampled three representative regions (A, B, and C), and analyzed the defect formation energies.

Here, all possible native point defects, i.e., three vacancies (V_{Cs}, V_{Pb}, V_{Br}), six antisites (Pb_{Cs}, Br_{Cs}, Cs_{Pb}, Br_{Pb}, Cs_{Br}, Pb_{Br}), and three interstitials (Cs_i, Pb_i, Br_i) were considered. For interstitial defects, we assumed the **6d** Wyckoff position for the initial configurations. We also tested site preference of V_{Cs}, Pb_{Cs}, and Br_{Cs} point defects at both **2a** and **6e** Wyckoff positions and we find that Cs at **2a** site is always favored (shows lower defect formation energy by $\sim 0.5\,\text{eV}$). Therefore, V_{Cs}, Pb_{Cs} and Br_{Cs} in the text refer those that occur at Cs at **2a** site. Calculated defect formation energies as a function of Fermi level are shown in Figure 3a-c where the self-consistent Fermi level is indicated as a dashed vertical line. Our results show that Pb_{Cs} and V_{Cs} are the dominant donor and acceptor defects that pin the Fermi level under all three conditions considered.

The concentration of native defects is predicted along the linear path A $\rightarrow$ B $\rightarrow$ C in Figure 1e and plotted in Figure 3d. While the concentration of most of low-energy (high-concentration) defect species remains constant along the path, the population of Br_{Cs} varies drastically. Under Br-rich / Cs, Pb-poor conditions (A point), the concentration of Br_{Cs} is $5 \times 10^{18}\,\text{cm}^{-3}$, which decreases to $3 \times 10^{-2}\,\text{cm}^{-3}$ under Br-poor / Cs, Pb-rich conditions. The concentrations of Pb_{Cs} and V_{Cs} remain around $10^{18}\,\text{cm}^{-3}$. The equilibrium carrier concentrations (Figure 3e) of $< 10^{9}\,\text{cm}^{-3}$ are much smaller than the defect concentrations due to a combination of strong compensation (charges of positive and negative defect cancel) and the fact that none of the defects considered are shallow donors or acceptors (see defect levels in Figure 2). This represents a severe case of intrinsic doping limits established for wide gap semiconducting compounds.[39,41,42] Pure crystals of Cs_4PbBr_6 in the dark are therefore predicted to be highly resistive. Full values for defect and carrier concentrations and Fermi level can be found in Table S2.

Optical transitions of point defects

Although analysis of the thermodynamic defect levels indicate traps within the band gap, this does not correspond to the photon energy associated with emission or absorption of radiation.

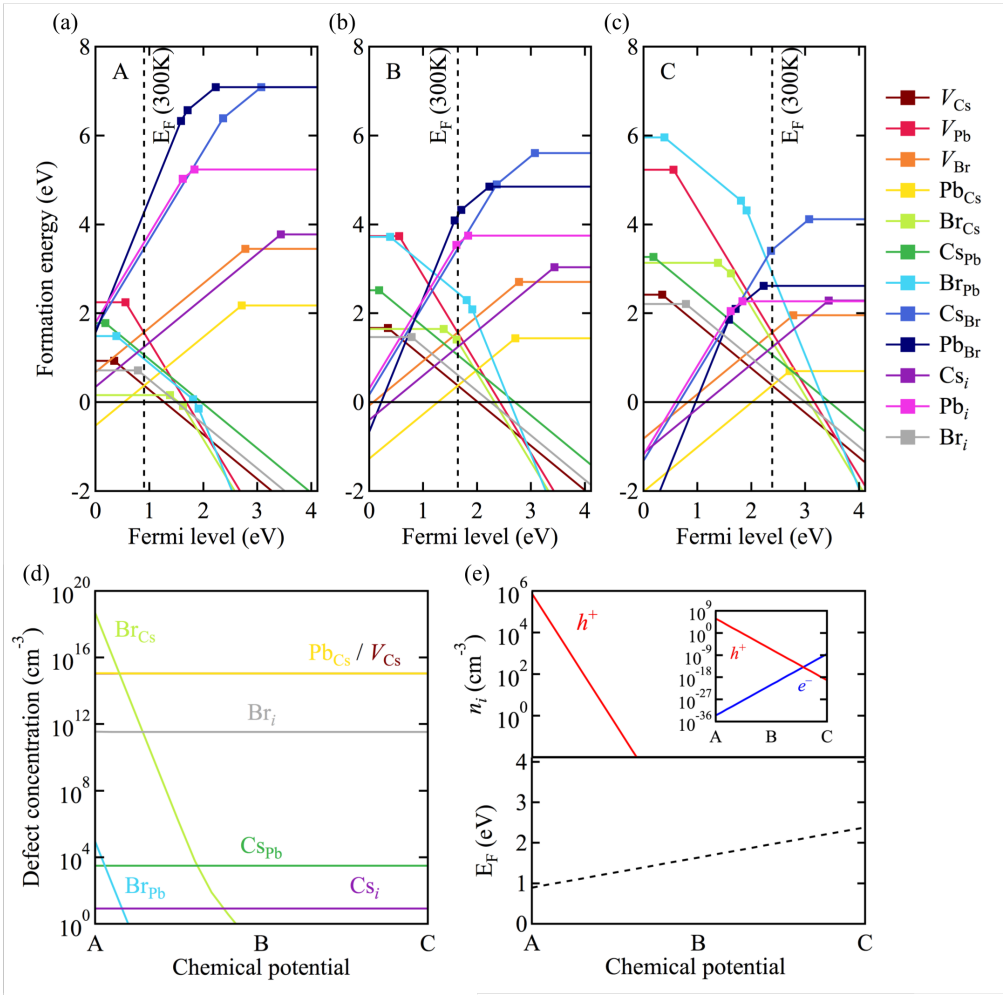

Figure 3: (a-c) Change of defect formation energies as a function of Fermi level at the chemical potential corresponding to given A, B, and C point in Figure 1e. Calculated self-consistent Fermi level is plotted as black dotted line. (d) Change of defect concentration, (e) carrier concentration, n_i, and Fermi level, E_F, as a function of chemical potential.

To understand the optical properties (fast response) it is necessary to consider the role of structural relaxation as described by configurational coordinate diagrams.[4,43] Here, we chose several key point defects including V_{Cs} and Pb_{Cs} as they are dominant acceptors and donors with high concentrations. V_{Br} has been suspected as a green emission center,[16,17] while Br_{Cs} is an interesting defect whose concentration can be tuned by changing the chemical potential. We also consider Br_i as it shows higher concentration than the remaining defect species.

In the dark, a defect will tend to adopt its lowest energy charge state at the equilibrium Fermi level, e.g. +1 for Pb_{Cs}. Upon illumination, capture or release of an electron from

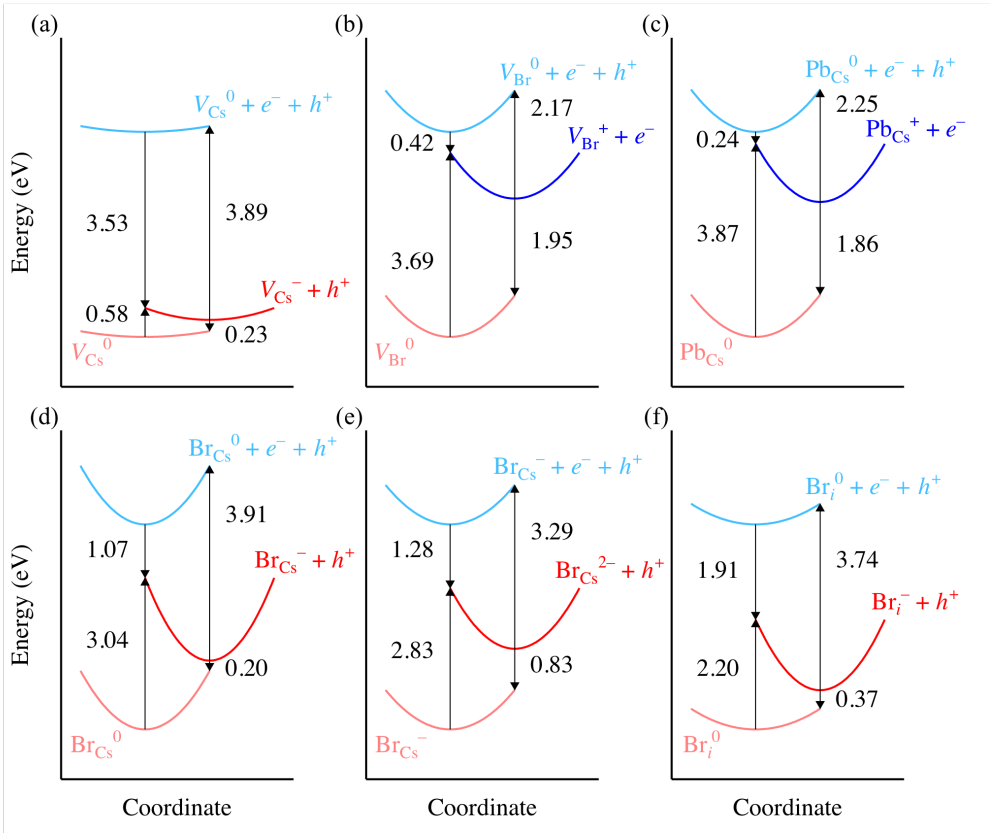

Figure 4: Calculated configurational coordinate diagram using the four-point method for one-carrier ionization processes of (a) V_{Cs}, (b) V_{Br}, (c) $\mathrm{Pb_{Cs}}$, (d-e) $\mathrm{Br_{Cs}}$, and (f) Br_i.

the semiconductor band edges can occur, which leads to one-carrier transitions described in Figure 4. These can be radiative or non-radiative depending on the nature of the potential energy surfaces involved. $\mathrm{Pb_{Cs}}$ has been suggested as a UV-emissive defect,[44] but we predict it will have much lower optical emission energy than the UV region. Rather V_{Cs} has the potential to emit UV light from the transition between the 0 and − charge states. Among all defect species considered above, only V_{Cs} shows weak electron-phonon coupling (small lattice relaxation), whereas the other defects show strong electron-phonon coupling (large lattice relaxation) during carrier capture process. From the range of defects and capture processes considered, green luminescence is not found.

Molecular behavior of the tribromide species

We now focus on Br_{Cs} as the only dominant native point defect whose concentration is controllable via changing growth or annealing conditions (chemical potential). The incorporation of excess bromine results in the formation of a Br_3 polybromide species, which is similar to molecular-like halide interstitials found in hybrid perovskites[45,46] and other metal halide systems.[1]

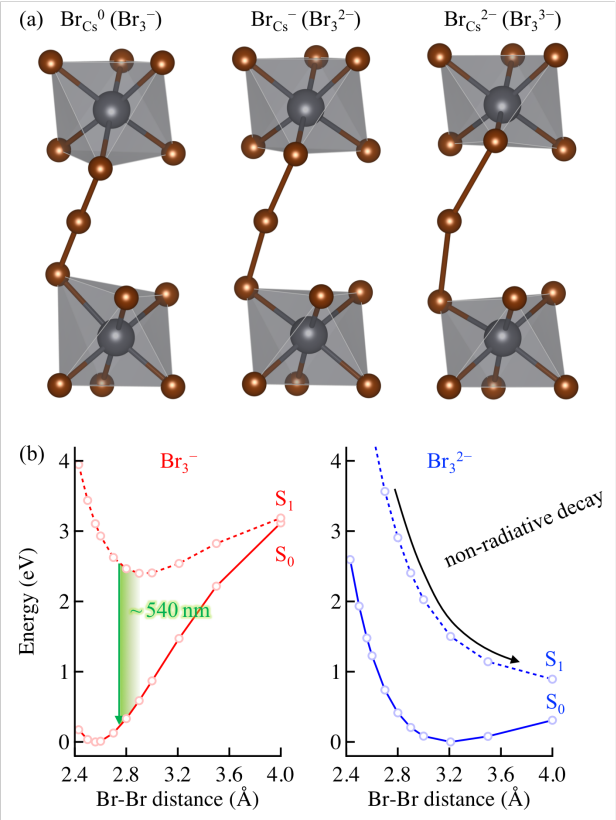

Figure 5: (a) The local structure associated with Br_{Cs}^{0} (Br_3^{-}), Br_{Cs}^{-} (Br_3^{2-}), and Br_{Cs}^{2-} (Br_3^{3-}) point defect species in Cs_4PbBr_6. (b) Ground state S_0 (solid line) and first excited state S_1 (dotted line) relative potential energy surfaces as a function of the Br–Br distance for Br_3^{-} (left) and Br_3^{2-} (right). Note that in a crystal environment the range of accessible Br–Br distances is limited in the 2.5 – 3.7 Årange.

The Br_{Cs} antisite is unconventional as, nominally, an anion (Br^-) substitutes a cation (Cs^+). However, inspection of the local structure around the defect reveals the formation of the Br_3 species: the substituted Br atom forms short bonds with neighbouring lattice Br^- ions. The *neutral* defect (Br_{Cs}^{0} in point defect notation) therefore corresponds to Br_3^{-} (with

Table 1: Calculated bond lengths (d_1 and d_2) in unit of Å and bond angle (θ) in unit of °.

	State	d_1	d_2	θ
Periodic crystal	Br_3^-	2.55	2.56	178.98
	Br_3^{2-}	3.09	3.11	171.27
	Br_3^{3-}	3.71	3.71	155.64
Embedded molecule	Br_3^-	2.56	2.56	180.00
	Br_3^{2-}	3.21	3.21	175.12
	Br_3^{3-}	14.14	14.45	130.70

spin $S = 0$). The negatively charged defect (Br_{Cs}^-) corresponds to Br_3^{2-} ($S = \frac{1}{2}$), while the doubly-negative defect (Br_{Cs}^{2-}) is Br_3^{3-} ($S = 0$). The local structure of the polybromides in Cs_4PbBr_6 are shown in Figure 5a. As these species gain electrons, a localized anti-bonding orbital is filled and, consequently, Br···Br bonds elongate (see Table 1 and Figure S3).

To shed light on the excited-state behavior of Br_3 in Cs_4PbBr_6, we adopted the molecule-in-crystal approach where Br_3 species were embedded in a dielectric medium ($\epsilon_0 = 8.05$) close to the calculated ϵ_0 of Cs_4PbBr_6.[45,47] For Br_3^-, good agreement is found between the bond lengths and angle from supercell defect calculations and those computed from embedded molecular calculations (see Table 1). However, Br_3^{2-} shows disagreement in their values with enlongation in the molecular case, which implies spatial confinement effect of Cs_4PbBr_6 crystals become larger for more negatively charged Br_3 (i.e. Br_3^{2-} and Br_3^{3-}). Moreover, it is found that Br_3^{3-} does not retain its molecular structure in a dielectric medium, whereas it remains stable in the Cs_4PbBr_6 crystal due to the steric confinement. All calculated values representing the ground-state molecular geometry of Br_3 species are tabulated in Table 1.

The presence of polybromide species (Br_3 or larger) may be inferred from their vibrational and optical signatures. We predict Br_3^- to have three characteristic vibrations in low frequency region: 78 cm^{-1} (ν_1); 156 cm^{-1} (ν_2); and 168 cm^{-1} (ν_3). These vibrations are softened as electrons are added to the anti-bonding orbitals and, consequently, Br_3^{2-} has peaks at 68 cm^{-1}, 83 cm^{-1}, and 94 cm^{-1}. Interestingly, the ν_3 modes of Br_3^-, and ν_2 and ν_3 modes of Br_3^{2-}, are Raman active and previous Raman measurements have observed peaks in this

range.[22,48] Calculation of bulk phonon modes of Cs_4PbBr_6 have found one at 86 cm^{-1} (near ν_2 of Br_3^{2-}), but none near ν_3 of Br_3^- or ν_3 of Br_3^{2-}.[44] This suggests that Raman peaks near 94 cm^{-1} and 168 cm^{-1} are not intrinsic vibrational modes but signatures of tribromide defects. The full range of frequencies and IR / Raman intensities are provided in Table S3 and Figure S4.

Beyond vibrational excitation, we next consider the optical excitation of these species. First, we analyzed the UV-Vis spectra using time-dependent DFT (Figure S5). Among the three species, only Br_3^- provides a low-lying singlet excitation (S_1) in the visible range: S_1 calculated at 401 nm (3.09 eV). This electronic transition is symmetry forbidden if the triatomic species is linear (internal angle of 180°). However, slight distortion from linearity is predicted in Cs_4PbBr_6 crystal due to its low energetic cost (Figure S6), which leads to a non-zero oscillator strength for S_1 in Br_3^- (Table S4). Both Br_3^{2-} and Br_3^{3-} are calculated with S_1 absorption far away from the green region: at 822 nm (1.51 eV) and 99 nm (12.54 eV), respectively.

Once excitation to S_1 from the Franck-Condon region occurs, excited-state geometry relaxation proceeds. We thus analyzed the lowest-lying electronic excitation energy as a function of the Br-Br distance. We restricted the scan to the range of bond lengths that was predicted in the crystal calculations (from 2.5 to 4.0 Å). Br_3^- and Br_3^{2-} provide S_1-S_0 energy differences in the range of green emission (ca. 2.3 eV or 540 nm) for the scanned Br–Br distances, whereas Br_3^{3-} shows too large S_1-S_0 gaps (Table S5 and Figure S7). The ground-state geometry for Br_3^{2-} provides a halogen−halogen distance of 3.21 Å, which already gives a too small S_1-S_0 energy gap (1.5 eV). Geometry relaxation of the first excited state of Br_3^{2-} would lead to an even smaller S_1-S_0 energy difference, thus promoting a non-radiative path to the ground state (Figure 5c right). In contrast, for Br_3^- the ground-state separation is 2.56 Å, which leads to an S_1-S_0 energy difference of 3.11 eV. While the S_1 state (Br–Br = 2.56 Å) undergoes non-radiative relaxation to its ground state (Br–Br = 2.8 and 2.9 Å), radiative relaxation to the S_0 state can occur with associated green luminescence (Figure 5b

left).

Non-radiative electronic relaxation through a conical intersection between S_1 and S_0 in Br_3^- is ruled out as an energy barrier of $> 0.5\,eV$ needs to be overcome. Our results, therefore, suggest the presence of a radiative mechanism with visible-light emission in Br_3^- molecular species that could explain the green fluorescence recorded in 0D perovskite Cs_4PbBr_6 upon tribromide defect formation. However, such defect-assisted luminescence cannot account for the *absorption* of green light in Cs_4PbBr_6. Therefore we can attribute the green absorption to $CsPbBr_3$ phase impurities alone, while emission could involve a combination of phase impurities and point defects.

Conclusions

The defect chemistry of the zero-dimensional Cs_4PbBr_6 perovskite is highly unusual. The low formation energy of the dominant donor (Pb_{Cs}) and acceptor (V_{Cs}) defects results in a high concentration of $10^{16}\,cm^{-3}$ at room temperature. Due to strong charge compensation, the material is predicted to be resistive with an excess hole concentration below $10^6\,cm^{-3}$ in the dark. This doping limit may be overcome under illumination or by finding extrinsic donors/acceptors with high solubility. In contrast to the 3D perovskites, and to recent speculation, the concentration of halide vacancies is shown to be negligible. The incorporation of excess bromine in the form of Br_{Cs} results in deep defect levels, and its concentration can be high or low depending on the growth condition. We show that this defect results in the formation of molecular Br_3-type species that exhibits a range of optical transitions in the visible range. Defect-mediated green luminescence can result from the fluorescence of optically excited Br_3^- to its ground state. The unique ability of halide ions to form aggregates with variable charge states likely plays a hidden role in the photochemistry of halide perovskite semiconductors, extending from carrier trapping, to electron-hole recombination, and luminescence.

Computational Methods

Density Functional Theory

Calculations of Cs_4PbBr_6 were performed based on Kohn-Sham density-functional theory[49] considering periodic boundary conditions. The Vienna Ab Initio Simulation Package (VASP)[50,51] was used with Projector augmented-wave (PAW)[52,53] pseudo-potentials where the valence states of Cs, Pb, and Br are treated explicitly by $9(5s^2 5p^6 6s^1)$, $14(5d^{10} 6s^2 6p^2)$ and $7(4s^2 4p^5)$ electrons, respectively. The Perdew-Burke-Ernzerhof exchange-correlation functional revised for solids (PBEsol)[54] was used to optimize structure of primitive unit cell (22 atoms) of Cs_4PbBr_6 with $4 \times 4 \times 4$ Γ-centered $\boldsymbol{k}$-mesh. We considered spin-orbit coupling (SOC) on PBEsol to calculate band structure and effective masses. For all PBEsol calculations, the plane-wave kinetic cutoff energy was set to 700 eV, while convergence criteria of 10^{-5} eV and $10^{-2}\,\mathrm{eV\AA^{-1}}$ for total energy and forces on each atoms were employed.

Defect Formation and Transitions

For defect calculations, a conventional hexagonal unit cell (66 atoms) of $CsPbBr_6$ was employed and perfect and defected unit cells were optimized within the same condition above. A $3 \times 3 \times 2$ Γ-centered $\boldsymbol{k}$-mesh was used. Since defect properties from scalar-relativistic PBEsol calculation are known to be inaccurate in perovskite system,[55] we performed single-shot self-consistent calculation using a non-local hybrid functional (HSE06)[56,57] with spin-orbit coupling (SOC) on PBEsol-optimized unit cells. Here, to save computational cost we reduced the plane-wave kinetic cutoff energy and the Brillouin zone (BZ) sampling to 400 eV and $2 \times 2 \times 2$, respectively. Finite-size corrections were also applied for charged defect supercell calculations using the calculated dielectric constant.[58,59] CPLAP and SC-FERMI package were used to calculate stability field in chemical potential space and self-consistent Fermi level, respectively.[60,61]

Excited States

For the electronic excitation of the tribromide defects, we performed time-dependent DFT molecular calculations at the hybrid PBE0/cc-pVTZ level of theory[62–64] by using the Gaussian-16.A03 suite of programs[65] for the Br_3 anionic species. Note that PBE0 and HSE06 are very similar in terms of functional formulation, the later using an error function screened Coulomb potential for the exchange part. We chose, however, the PBE0 functional for the optical properties of the embedded system as it has been largely tested and shown slightly better accuracy for excited state predictions.[66] In order to simulate the perovskite environment in the molecular calculations, the self-consistent reaction field approximation was employed through the polarizable continuum solvent model (PCM)[67,68] with a solvent that matches the dielectric constant of the 0D perovskite Cs_4PbBr_6 (1-bromopropane, $\epsilon = 8.05$). First, minimum energy geometries were obtained for Br_3^-, Br_3^{2-} and Br_3^{3-}. Their absorption spectra were simulated by calculating the 30 lowest same-spin electronic excitations at the TD-PBE0/cc-pVTZ+PCM level, and the first electronic transition energy was scanned as a function of the Br-Br distance. In the scan, the minimum-energy internal angle for the ground state was kept fixed, and both Br-Br bond lengths were varied simultaneously in a range of values between 2.5 and 4.0 Å.

Data Access

The crystal structure files for the optimized pristine and defective materials have been made available in an on-line repository at https://doi.org/10.5281/zenodo.2641358. The other input and output files are available upon request.

Acknowledgement

The authors thank S. D. Stranks and M. V. Kovalenko for useful discussions. This research was supported by Young Researcher Program and Creative Materials Discovery Pro-

gram through the National Research Foundation of Korea (NRF) funded by Ministry of Science and ICT (2018R1C1B6008728 and 2018M3D1A1058536). We are grateful to the UK Materials and Molecular Modelling Hub for computational resources, which is partially funded by EPSRC (EP/P020194/1). JC acknowledges the Generalitat Valenciana for the APOSTD/2017/081 fellowship.

References

(1) Hayes, W.; Stoneham, A. M. *Defects and defect processes in nonmetallic solids*; Wiley, 1985.

(2) Ehret, W.; Greenstone, A. *J. Am. Chem. Soc.* **1943**, *65*, 872–877.

(3) Buckeridge, J.; Catlow, C. R. A.; Scanlon, D.; Keal, T.; Sherwood, P.; Miskufova, M.; Walsh, A.; Woodley, S.; Sokol, A. *Phys. Rev. Lett.* **2015**, *114*, 016405.

(4) Huang, K.; Rhys, A. *Proc. Royal Soc. A* **1950**, *204*, 406–423.

(5) Park, J.-S.; Kim, S.; Xie, Z.; Walsh, A. *Nat. Rev. Mater.* **2018**, *3*, 194–210.

(6) Kojima, A.; Teshima, K.; Shirai, Y.; Miyasaka, T. *J. Am. Chem. Soc.* **2009**, *131*, 6050–6051.

(7) Lee, M. M.; Teuscher, J.; Miyasaka, T.; Murakami, T. N.; Snaith, H. J. *Science* **2012**, *338*.

(8) Stoumpos, C. C.; Soe, C. M. M.; Tsai, H.; Nie, W.; Blancon, J.-C.; Cao, D. H.; Liu, F.; Traor, B.; Katan, C.; Even, J.; Mohite, A. D.; Kanatzidis, M. G. *Chem* **2017**, *2*, 427–440.

(9) Saidaminov, M. I.; Almutlaq, J.; Sarmah, S.; Dursun, I.; Zhumekenov, A. A.; Begum, R.; Pan, J.; Cho, N.; Mohammed, O. F.; Bakr, O. M. *ACS Energy Lett.* **2016**, *1*, 840–845.

(10) Benin, B. M.; Dirin, D. N.; Morad, V.; Wörle, M.; Yakunin, S.; Rainò, G.; Nazarenko, O.; Fischer, M.; Infante, I.; Kovalenko, M. V. *Angew. Chem. Int. Ed.* **2018**, *130*, 11499–11503.

(11) Akkerman, Q. A.; Park, S.; Radicchi, E.; Nunzi, F.; Mosconi, E.; De Angelis, F.; Brescia, R.; Rastogi, P.; Prato, M.; Manna, L. *Nano Lett.* **2017**, *17*, 1924–1930.

(12) Andrews, R. H.; Clark, S. J.; Donaldson, J. D.; Dewan, J. C.; Silver, J. *J. Chem. Soc. Dalton Trans.* **1983**, *0*, 767–770.

(13) Nikl, M.; Mihokova, E.; Nitsch, K.; Somma, F.; Giampaolo, C.; Pazzi, G. P.; Fabeni, P.; Zazubovich, S. *Chem. Phys. Lett.* **1999**, *306*, 280–284.

(14) Quan, L. N.; Quintero-Bermudez, R.; Voznyy, O.; Walters, G.; Jain, A.; Fan, J. Z.; Zheng, X.; Yang, Z.; Sargent, E. H. *Adv. Mater.* **2017**, *29*.

(15) Chen, X.; Zhang, F.; Ge, Y.; Shi, L.; Huang, S.; Tang, J.; Lv, Z.; Zhang, L.; Zou, B.; Zhong, H. *Adv. Funct. Mater.* **2018**, *28*, 1706567.

(16) De Bastiani, M. et al. *Chem. Mater.* **2017**, *29*, 7108–7113.

(17) Yin, J.; Yang, H.; Song, K.; El-Zohry, A. M.; Han, Y.; Bakr, O. M.; Bredas, J.-L.; Mohammed, O. F. *J. Phys. Chem. Lett.* **2018**, *9*, 5490–5495.

(18) Seth, S.; Samanta, A. *J. Phys. Chem. Lett.* **2018**, *9*, 176–183.

(19) Han, D.; Shi, H.; Ming, W.; Zhou, C.; Ma, B.; Saparov, B.; Ma, Y.-Z.; Chen, S.; Du, M.-H. *J. Mater. Chem. C* **2018**, *6*, 6398–6405.

(20) Akkerman, Q. A.; Abdelhady, A. L.; Manna, L. *J. Phys. Chem. Lett.* **2018**, *9*, 2326–2337.

(21) Almutlaq, J.; Yin, J.; Mohammed, O. F.; Bakr, O. M. *J. Phys. Chem. Lett.* **2018**, *9*, 4131–4138.

(22) Velázquez, M.; Ferrier, A.; Péchev, S.; Gravereau, P.; Chaminade, J.-P.; Portier, X.; Moncorgé, R. *J. Cryst. Growth* **2008**, *310*, 5458–5463.

(23) Kang, B.; Biswas, K. *J. Phys. Chem. Lett.* **2018**, *9*, 830–836.

(24) Birch, F. *Phys. Rev.* **1947**, *71*, 809–824.

(25) Jung, Y.-K.; Butler, K. T.; Walsh, A. *J. Phys. Chem. C* **2017**, *121*, 27351–27356.

(26) Whalley, L. D.; Frost, J. M.; Morgan, B. J.; Walsh, A. *Phy. Rev. B* **2019**, *99*, 085207.

(27) Baroni, S.; de Gironcoli, S.; Corso, A. D.; Giannozzi, P. *Rev. Mod. Phys.* **2001**, *73*, 515–562.

(28) Brivio, F.; Walker, A. B.; Walsh, A. *APL Mater* **2013**, *1*, 042111.

(29) Whalley, L. D.; Frost, J. M.; Jung, Y.-K.; Walsh, A. *J. Chem. Phys.* **2017**, *146*, 220901–12.

(30) Jung, Y.-K.; Lee, J.-H.; Walsh, A.; Soon, A. *Chem. Mater.* **2017**, *29*, 3181–3188.

(31) Zhang, Y.; Saidaminov, M. I.; Dursun, I.; Yang, H.; Murali, B.; Alarousu, E.; Yengel, E.; Alshankiti, B. A.; Bakr, O. M.; Mohammed, O. F. *J. Phys. Chem. Lett.* **2017**, *8*, 961–965.

(32) Akkerman, Q. A.; Gandini, M.; Di Stasio, F.; Rastogi, P.; Palazon, F.; Bertoni, G.; Ball, J. M.; Prato, M.; Petrozza, A.; Manna, L. *Nat. Energy* **2016**, *2*, 2225.

(33) Zhang, Y.; Yu, F.-X.; Ma, X.-J.; Xiong, Z.-Y.; Wang, Z.-Q.; Chen, P.; Xiong, Z.-H.; Gao, C.-H. *Org. Electron.* **2017**, *50*, 411–417.

(34) Endres, J.; Kulbak, M.; Zhao, L.; Rand, B. P.; Cahen, D.; Hodes, G.; Kahn, A. *J. Appl. Phys.* **2017**, *121*, 035304.

(35) Ng, C. H.; Ripolles, T. S.; Hamada, K.; Teo, S. H.; Lim, H. N.; Bisquert, J.; Hayase, S. *Scientific Reports* **2018**, *8*, 2482.

(36) Park, J.-S.; Jung, Y.-K.; Butler, K. T.; Walsh, A. *J. Phys. Energy* **2019**, *1*, 016001.

(37) Riesen, N.; Lockrey, M.; Badek, K.; Riesen, H. *Nanoscale* **2019**, *11*, 3925–3932.

(38) Freysoldt, C.; Grabowski, B.; Hickel, T.; Neugebauer, J.; Kresse, G.; Janotti, A.; Van de Walle, C. G. *Rev. Mod. Phys.* **2014**, *86*, 253–305.

(39) Walsh, A.; Zunger, A. *Nat. Mater.* **2017**, *16*, 964–967.

(40) Kondo, S.; Amaya, K.; Saito, T. *J. Phys.: Condens. Matter* **2002**, *14*, 2093–2099.

(41) Zhang, S.; Wei, S.-H.; Zunger, A. *Phys. Rev. Lett.* **2000**, *84*, 1232.

(42) Van de Walle, C. G.; Laks, D.; Neumark, G.; Pantelides, S. *Phys. Rev. B* **1993**, *47*, 9425.

(43) Stoneham, A. M. *Theory of Defects in Solids*; Oxford University Press, Oxford, 1975.

(44) Yin, J.; Zhang, Y.; Bruno, A.; Soci, C.; Bakr, O. M.; Bredas, J.-L.; Mohammed, O. F. *ACS Energy Lett.* **2017**, *2*, 2805–2811.

(45) Whalley, L. D.; Crespo-Otero, R.; Walsh, A. *ACS Energy Lett.* **2017**, *2*, 2713–2714.

(46) Meggiolaro, D.; Motti, S. G.; Mosconi, E.; Barker, A. J.; Ball, J.; Perini, C. A. R.; Deschler, F.; Petrozza, A.; De Angelis, F. *Energy Environ. Sci.* **2018**, *11*, 702–713.

(47) Tasker, P. W.; Stoneham, A. M. *J. Phys. Chem. Solids* **1977**, *38*, 1185–1189.

(48) Cha, J.-H.; Han, J. H.; Yin, W.; Park, C.; Park, Y.; Ahn, T. K.; Cho, J. H.; Jung, D.-Y. *J. Phys. Chem. Lett.* **2017**, *8*, 565–570.

(49) Kohn, W.; Sham, L. J. *Phys. Rev.* **1965**, *140*, A1133–A1138.

(50) Kresse, G.; Furthmüller, J. *Phys. Rev. B* **1996**, *54*, 11169–11186.

(51) Kresse, G.; Furthmüller, J. *Comput. Mater. Sci.* **1996**, *6*, 15–50.

(52) Kresse, G.; Joubert, D. *Phys. Rev. B* **1999**, *59*, 1758–1775.

(53) Blöchl, P. E. *Phys. Rev. B* **1994**, *50*, 17953–17979.

(54) Perdew, J. P.; Ruzsinszky, A.; Csonka, G. I.; Vydrov, O. A.; Scuseria, G. E.; Constantin, L. A.; Zhou, X.; Burke, K. *Phys. Rev. Lett.* **2008**, *100*, 136406.

(55) Du, M.-H. *J. Phys. Chem. Lett.* **2015**, *6*, 1461–1466.

(56) Heyd, J.; Scuseria, G. E.; Ernzerhof, M. *J. Chem. Phys.* **2003**, *118*, 8207–8215.

(57) Krukau, A. V.; Vydrov, O. A.; Izmaylov, A. F.; Scuseria, G. E. *J. Chem. Phys.* **2006**, *125*, 224106.

(58) Freysoldt, C.; Neugebauer, J.; Van de Walle, C. G. *Phys Rev. lett.* **2009**, *102*, 016402.

(59) Kumagai, Y.; Oba, F. *Phys. Rev. B* **2014**, *89*.

(60) Buckeridge, J.; Scanlon, D. O.; Walsh, A.; Catlow, C. R. A. *Comput. Phys. Commun.* **2014**, *185*, 330–338.

(61) SC-FERMI. `https://github.com/jbuckeridge/sc-fermi`, (accessed April 23, 2019).

(62) Dunning, T. H. *J. Chem. Phys.* **1989**, *90*, 1007–1023.

(63) Kendall, R. A.; Dunning, T. H.; Harrison, R. J. *J. Chem. Phys.* **1992**, *96*, 6796–6806.

(64) Adamo, C.; Barone, V. *J. Chem. Phys.* **1999**, *110*, 6158–6170.

(65) Frisch, M. J. et al. Gaussian16 Revision A.03. 2016; Gaussian Inc. Wallingford CT.

(66) Laurent, A. D.; Jacquemin, D. *International Journal of Quantum Chemistry* **2013**, *113*, 2019–2039.

(67) Cossi, M.; Barone, V.; Cammi, R.; Tomasi, J. *Chem. Phys. Lett.* **1996**, *255*, 327–335.

(68) Mennucci, B.; Tomasi, J. *J. Chem. Phys.* **1997**, *106*, 5151–5158.